

Multiple-Beam Surface Plasmon Holographic Nanolithography

Qiuqun Liang · Weixing Yu · Taisheng Wang · Hua Liu ·
Wenbin Xu · Renguan Piao · Yongqi Fu

Received: 27 March 2012 / Accepted: 13 August 2012 / Published online: 30 August 2012
© Springer Science+Business Media, LLC 2012

Abstract Multiple-beam surface plasmon holographic nanolithography based on a hemispherical prism coupling configuration is numerically studied in this paper. The proposed configuration is systematically analyzed and optimized for the purpose of achieving five different two-dimensional Bravais lattices by means of adjusting the spatial distribution of three incident beams properly. Furthermore, it is shown that the variation in the relative phase between incident beams can give rise to rich periodic patterns when overlapping more than three beams for surface plasmon holographic nanolithography.

Keywords Surface plasmon · Multiple-beam holographic nanolithography · 2-D Bravais lattices

Introduction

Holographic lithography has been proved to be a powerful, cost-effective, and promising technique to fabricate various periodic and quasi-periodic structures without requiring any

fine periodic masks. Laser holographic lithography, also called laser interference lithography, as a large-area, maskless, and noncontact nanofabrication technique, has been well developed recently to obtain one-dimensional grating lines, two-dimensional (2-D) array of square lattices, nanowires, nanofins or nanowires with oval cross sections [1–5], and three-dimensional photonic crystals [6–12]. These nanostructures were put forth in high demand for a wide range of applications including surface relief gratings, biosensors, large-volume photonic crystal templates, photonic crystal waveguides, high-density data storage, nanoelectronic devices, and integrated circuits. However, this conventional holographic lithographic method is unable to fabricate high-resolution structures due to the optical diffraction limit. By introducing near-field optical lithography technique, the diffraction limit can be broken and super resolution can be achieved. Evanescent wave interference lithography, as one of the near-field interference lithographic methods, can provide high resolution but has the intrinsic disadvantages including short exposure depth, low contrast, and others to limit its practical applications [13–16]. However, by exciting surface plasmon waves resulting from the coupling of light to collective free-electron mode at metal/dielectric interface, the evanescent field can be strongly enhanced with the improved resolution as well. Surface plasmon interference nanolithography (SPIN), as a promising near-field nanolithography technique, has shown its distinctive superiority in unlimited resolution and thus been rapidly developed recently. Periodic nanolines and nanodot arrays with a sub-30-nm resolution fabricated by means of SPIN technique have been demonstrated numerically and experimentally recently [17–24].

To meet the requirements of high-resolution periodic patterns in various fields, such as biosensors, metamaterials, photonic crystals, magnetic data storage, and field emitter arrays, surface plasmon holographic nanolithography based on prism coupling is studied in the paper so as to achieve a variety of 2-D photonic crystals template with high resolution and aspect ratio.

Q. Liang · W. Yu (✉)
State Key Laboratory of Applied Optics,
Changchun Institute of Optics, Fine Mechanics and Physics,
Chinese Academy of Sciences,
Changchun, Jilin 130033, China
e-mail: yuwx@ciomp.ac.cn

Q. Liang
Graduate University of Chinese Academy of Sciences,
Beijing 10039, China

T. Wang · H. Liu · W. Xu · R. Piao
Opto-electronic Technology Center,
Changchun Institute of Optics, Fine Mechanics and Physics,
Chinese Academy of Sciences,
Changchun, Jilin 130033, China

Y. Fu (✉)
School of Physical Electronics,
University of Electronic Science and Technology of China,
Chengdu 610054, Sichuan Province, People's Republic of China
e-mail: yqfu@uestc.edu.cn

Theoretical Analysis

Basic Configuration and the Principle of SP Holography

Surface plasmons (SPs) are coherent electron oscillations that exist at the interface between conductors and dielectrics. The dispersion relation for the surface plasmons is given by [25],

$$k_{sp} = k_0 \sqrt{\frac{\epsilon'_m \epsilon_d}{\epsilon'_m + \epsilon_d}} \tag{1}$$

Where k_0 and k_{sp} are, respectively, the wave vectors of the incident light and the surface plasmons. ϵ'_m is the real part of the dielectric constant of metal, and ϵ_d is the dielectric constant of the dielectric medium. The wavelength of the surface plasmons can be written as,

$$\lambda_{sp} = \frac{2\pi}{k_{sp}} = \lambda_0 \sqrt{\frac{\epsilon'_m + \epsilon_d}{\epsilon'_m \epsilon_d}} \tag{2}$$

where λ_0 and λ_{sp} are, respectively, the wavelengths of the illumination light and the surface plasmons. By choosing proper dielectric constants of the metal film and dielectric medium, as well as the illumination wavelength, the wavelength of the SP wave can be much smaller than that of the incident light; thus, the resolution of SP holography can be significantly improved in comparison with the traditional laser holography. Meanwhile, the period of the SP interference pattern depends on the wavelength of the incident light and the material chosen.

The SP holographic nanolithography studied here is performed on the basis of the Kretschman’s attenuated total reflection principle [25, 26], where surface plasmons can be excited when the p -polarized light satisfies the following dispersion relation,

$$k_x = k_0 \sqrt{\epsilon_p} \sin \theta_{sp} = k_{sp} = k_0 \sqrt{\frac{\epsilon'_m \epsilon_d}{\epsilon'_m + \epsilon_d}} \tag{3}$$

where k_x represents the wave vector of the incident light projected on the plane parallel to the surface of the metal. ϵ_p is the dielectric constant of the prism, and θ_{sp} is the surface plasmon resonance angle.

In our simulation, the wavelength of the incident light is 365 nm. The dielectric constants of the prism, metal, and photoresist are 3.7605 (N-LASF31A glass), $-19.459 + 3.606i$ (Al) [27], and 3.0109 (S1813), respectively. Surface plasmon resonance angle at the interface of the prism and the metal surface by theoretical calculation is 76.7° . Thus, the wavelength of the surface plasmon is about 193 nm.

A schematic diagram of surface plasmon holographic lithography configuration is shown in Fig. 1. This configuration is composed of a hemispherical prism coated with a thin metal

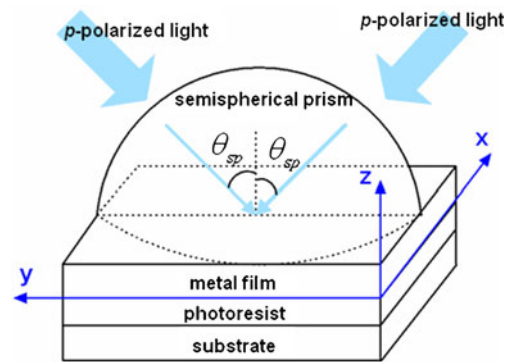


Fig. 1 Schematic diagram of SP holographic nanolithography configuration

layer and a photoresist coated on the substrate. We choose hemispherical prism for the sake of the flexibility of tuning the spatial distribution of the incident beams and the relative phase differences among these different incident beams in the practical application.

Electric field distribution of multiple-beam surface plasmon holographic lithography

By solving the Maxwell’s curl equations, the distribution of the electromagnetic field of the surface plasmon holographic interference patterns in the photoresist layer can be obtained. When the p -polarized plane wave propagates along the X -direction, there is no Y electric component. Thus, both the electric and magnetic field in the photoresist can be described as follows,

$$(E_{x,sp}, H_{y,sp}, E_{z,sp}) = (E_{3x}, H_{3y}, E_{3z}) e^{i(k_x x - k_{3z} z - \omega t)} \tag{4}$$

where k_x is the wave vector component along X -direction below the metal film, and k_{3z} is the wave vector component along Z -direction in the photoresist layer. They can be written as [25],

$$k_x = k_{sp} = \frac{\omega}{c} \sqrt{\frac{\epsilon'_m \epsilon_d}{\epsilon'_m + \epsilon_d}} \tag{5}$$

$$k_{3z} = \sqrt{\epsilon_d \left(\frac{\omega}{c}\right)^2 - k_x^2} = \frac{\omega}{c} \sqrt{\frac{\epsilon_d^2}{\epsilon'_m + \epsilon_d}} \tag{6}$$

Since $\epsilon_d^2 > 0$ and $|\epsilon'_m| > \epsilon_d$, k_{3z} is imaginary, and it can be expressed as $k_{3z} = -ik$, here k is a real number. Hence [18, 21],

$$\begin{aligned} H_{3y}(x, z) &= |H_{3y}| e^{-ik_{3z} z} e^{ik_x x} \\ &= |H_{3y}| e^{-kz} \cos(k_x x - \omega t) \end{aligned} \tag{7}$$

$$\begin{aligned}
 E_{x,sp}(x, z) &= -\frac{H_{y,sp}k_{3z}}{\omega\varepsilon_0\varepsilon_3} \\
 &= -\frac{|H_{3y}|k_z}{\omega\varepsilon_0\varepsilon_3} e^{-kz} \sin(k_x x - \omega t)
 \end{aligned}
 \tag{8}$$

$$\begin{aligned}
 E_{z,sp}(x, z) &= -\frac{H_{y,sp}k_x}{\omega\varepsilon_0\varepsilon_3} \\
 &= -\frac{|H_{3y}|k_x}{\omega\varepsilon_0\varepsilon_3} e^{-kz} \cos(k_x x - \omega t)
 \end{aligned}
 \tag{9}$$

where $|H_{3y}|$ is the field amplitude in the photoresist layer.

It can be seen from Eqs. (8) and (9) that the amplitude of $E_{x,sp}$ and $E_{z,sp}$ components exponentially decays due to the item of $\exp(-|k||z|)$, and the amplitude ratio is given by,

$$\frac{|E_{z,sp}|}{|E_{x,sp}|} = \frac{|k_x|}{|k_{3z}|} = \sqrt{\frac{|\varepsilon'_m|}{\varepsilon_d}}
 \tag{10}$$

The field component $E_{z,sp}(x,y,z)$ should dominate over the $E_{x,sp}(x,z,t)$ component to provide sufficient intensity contrast because there is a phase difference of $\frac{\pi}{2}$ existing between $E_{x,sp}(x,z,t)$ and $E_{z,sp}(x,z,z)$, which will give rise to a shift of a half-period in space between these two electric components. Furthermore, when the incident light propagates along Y -direction, there is no X electric component, and the electromagnetic field in the photoresist is similar. Therefore, the intensity of the multi-beam surface plasmon interference in the photoresist layer can be described as,

$$I_{z,sp} \propto (|E_{z,sp,1} + E_{z,sp,2} + \dots + E_{z,sp,n}|)^2
 \tag{11}$$

The intensity distribution of multiple noncoplanar beams interference can be described as [12],

$$\begin{aligned}
 I &= \sum_i E_i^2 + \sum_{i<j} 2E_i E_j \cos \theta_{ij} \cos \left[(\vec{k}_i - \vec{k}_j) \cdot \vec{r} + \varphi_{oi} - \varphi_{oj} \right], \\
 i, j &= 1, 2, 3 \dots
 \end{aligned}
 \tag{12}$$

where E_i, \vec{k}_i , and φ_{oi} are the plane wave’s amplitude, wave vector, and initial phase, respectively, θ_{ij} is the angle between \vec{k}_i and \vec{k}_j , and \vec{r} is the position vector.

For SP holography, the wave vector \vec{k}_{sp} of the SP waves are all lying at the interface of the metal film and the photoresist layer (within X - Y plane), and thus they are always coplanar. Note that the incident angle of each beam is set as the excitation angle of the surface plasmon resonance. Different azimuth angles of the incident light will directly result in different directions of the SP waves. And hence, the SP interference pattern can be controlled by means of

modulating the field amplitudes, the spatial distributions, the wave vectors, and the phases of the incident light beams.

The Theoretical Analysis of all Five 2-D Bravais Lattices Formed by SP Holography

There are five Bravais lattices in two dimensions, and they are square, hexagonal, centered rectangular (rhombic), rectangular, and oblique. The propagation vectors \vec{k}_1, \vec{k}_2 and \vec{k}_3 for three noncoplanar laser beams used to generate five 2-D Bravais lattices by holography are illustrated in Fig. 2a. For convenience, we use spherical coordinate system here. θ_i is the polar angle, and ϕ_i is the azimuth angle. The resulting lattices formed by maximum intensity points are illustrated in Fig. 2c. \vec{a}_1 and \vec{a}_2 are the primitive vectors that span the lattice, a and b are the real-space lattice constants along \vec{a}_1 and \vec{a}_2 directions, and γ is the angle between the primitive vectors. The lattice constants of 2-D Bravais lattices generated by this technique can be expressed as [11],

$$a \equiv |\vec{a}_1| = \frac{\lambda}{|\sin \theta (\cos \phi_1 - \cos \phi_2)|}
 \tag{13}$$

$$b \equiv |\vec{a}_2| = \frac{\lambda}{2|\sin \theta \sin \phi_2 \sin((\phi_1 + \phi_2)/2)|}
 \tag{14}$$

$$\gamma \equiv \cos^{-1} \left(\frac{\vec{a}_1 \cdot \vec{a}_2}{ab} \right) = \frac{\phi_1 + \phi_2}{2}
 \tag{15}$$

where λ is the wavelength of the incident beams, and the polar angles have the relation of $\theta_1 = \theta_2 = \theta_3 = \theta$, the azimuth angles have the relation of $\phi_2 = -\phi_3$.

For the SP holography, it is noted that the wave vectors k_{sp} of the SP waves are coplanar as illustrated in the Fig. 2b. Hence, in Eqs. (13) and (14), $\theta = \frac{\pi}{2}$, $\sin \theta = 1$, and the lattice constant can be described as,

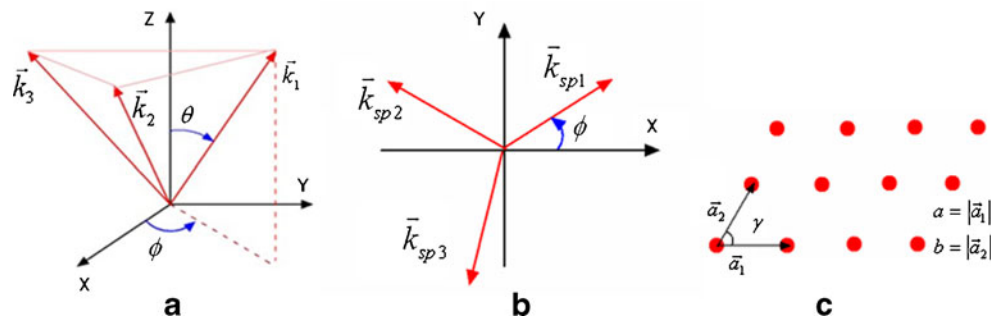
$$a \equiv |\vec{a}_1| = \frac{\lambda_{sp}}{|\cos \phi_1 - \cos \phi_2|}
 \tag{16}$$

$$b \equiv |\vec{a}_2| = \frac{\lambda_{sp}}{2|\sin \phi_2 \sin((\phi_1 + \phi_2)/2)|}
 \tag{17}$$

$$\gamma \equiv \cos^{-1} \left(\frac{\vec{a}_1 \cdot \vec{a}_2}{ab} \right) = \frac{\phi_1 + \phi_2}{2}
 \tag{18}$$

In practice, the wavelength λ_{sp} of the SP wave and the desired lattice parameters a, b , and γ are often known, so the azimuth angles can be found using the following three expressions,

Fig. 2 **a** The spatial distribution of three noncoplanar propagation vectors for laser holography, **b** the spatial distribution of three SP wave vectors for SP holography, and **c** the resulting lattice



$$\tan \phi_2 = \frac{\sin \gamma}{\cos \gamma - \frac{b}{a}} \tag{19}$$

$$\phi_1 = 2\gamma - \phi_2 \tag{20}$$

$$\phi_3 = -\phi_2 \tag{21}$$

A summary of the required azimuth angles and the resulting lattice constants of five 2-D Bravais crystals formed by SP holography can be seen in Table 1.

Results and Discussions

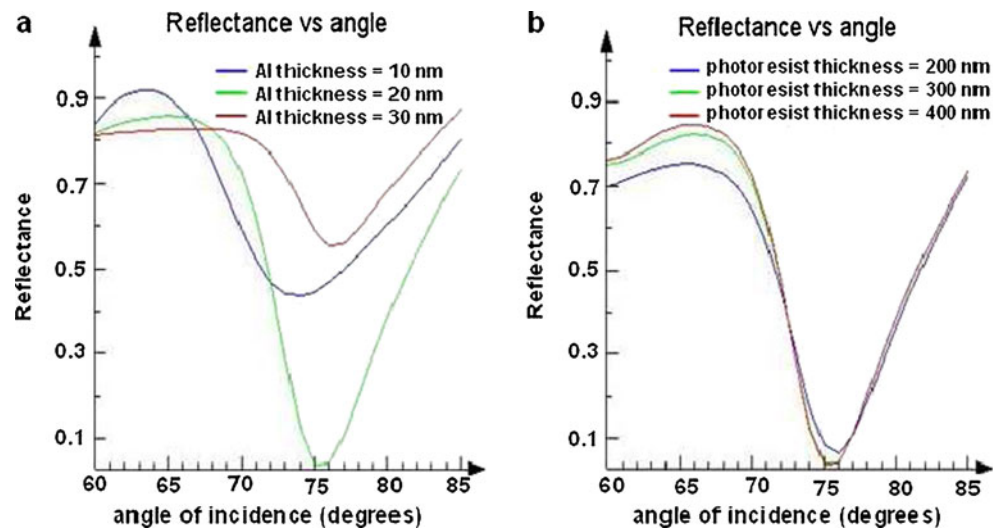
The finite-difference and time-domain (FDTD) algorithm is employed to numerically analyze multiple-beam SP holographic nanolithography. Perfectly matched layer boundary condition is used along the z-axis, and Bloch boundary condition is used along the other axes. Z-axis is taken as the decay direction, and the origin point (z=0) is set at the metal/photoresist interface. Further

analysis reveals that the field enhancement and the contrast of the SP interference pattern are affected by the thickness of the metal film and the incident angle of the light. When the thickness of the metal film and the incident angle are optimized to make the reflectance reach zero, the maximum incident light will be effectively coupled into collective free-electron mode at metal/dielectric interface; thus, surface plasmons are excited and the transmission can be enhanced significantly [25]. In this work, both the thicknesses of the metal film and the photoresist layer are optimized to find out the SP resonance angle θ_{SP} . The simulation results shown in Fig. 3a, b indicate that when the Al thickness is ~20 nm and the photoresist thickness is around 300 nm, the reflectance reaches nearly zero, and the optimum θ_{SP} is around 76° accordingly, which is in accordance with the theoretical analysis. Comparing with Fig. 3a and b, it is apparent that the thickness of the metal film has more significant effect on the reflectance than that of the photoresist layer. As can be seen from Fig. 3a, the thickness of the metal film should be chosen carefully as thicker or thinner of metal film will affect the reflectance dramatically. Here, the optimum

Table 1 Required azimuth angles and the resulting lattice constants of five 2-D Bravais crystals formed by SP holography

Bravais lattices					
Bravais lattices constants	Square $a = b, \gamma = \frac{\pi}{2}$	Rectangular $a \neq b, \gamma = \frac{\pi}{2}$ (e.g. $a = \sqrt{3}b$)	Rhombic $a = b, \gamma \neq \frac{\pi}{2}, \frac{2\pi}{3}$ (e.g. $\gamma = \frac{\pi}{6}$)	Hexagonal $a = b, \gamma = \frac{\pi}{3}$	Oblique $a \neq b, \gamma \neq \frac{\pi}{2}, \frac{2\pi}{3}$ (e.g. $b = \sqrt{3}a, \gamma = \frac{\pi}{6}$)
Required azimuth angles	$(\frac{\pi}{4}, \frac{3\pi}{4}, -\frac{3\pi}{4})$	$(\frac{\pi}{3}, \frac{2\pi}{3}, -\frac{2\pi}{3})$	$(-\frac{\pi}{4}, \frac{7\pi}{12}, -\frac{7\pi}{12})$	$(0, \frac{2\pi}{3}, -\frac{2\pi}{3})$	$(-\frac{\pi}{2}, \frac{5\pi}{6}, -\frac{5\pi}{6})$
Resulting lattice constants	$a = b = 0.707\lambda_{sp}$ $= 136nm$	$a = \lambda_{sp} = 193nm$ $b = 0.577\lambda_{sp} = 111nm$	$a = b = 1.035\lambda_{sp}$ $= 200nm$	$a = b = 0.667\lambda_{sp}$ $= 129nm$	$a = 1.155\lambda_{sp} = 223nm$ $b = 2\lambda_{sp} = 396nm$

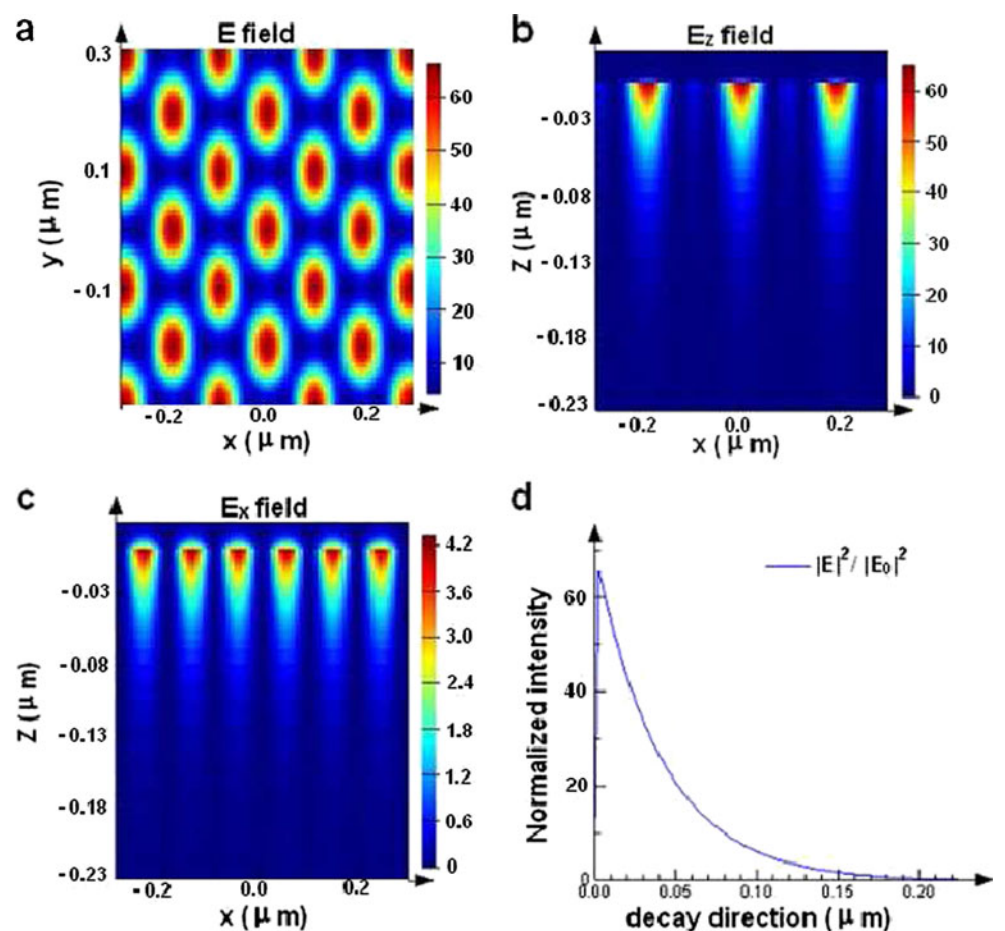
Fig. 3 SP resonance angle calculation using the FDTD solution: reflectance versus incident angle. **a** Optimize the incident angle and the thickness of metal film. **b** Optimize the incident angle and the thickness of photoresist layer



thickness of metal film is about 20 nm, and a fluctuation of 10 nm on the thickness will result in an increase of more than 45 % of reflectance. If more incident light is reflected back, it means that less collective free

electrons will be excited and coupled with the incident light [25]. Therefore, it is critical to select the optimum thickness of the metal film to achieve the maximum enhancement of the coupled electromagnetic field.

Fig. 4 Electric field distribution of three-beam SP interference pattern generated on the photoresist layer. The azimuth angles of the incident light are 0, $\pi/2$ and π , respectively. **a** E field in X-Y plane. **b** E_z field in X-Z plane. **c** E_x field in X-Z plane. **d** Normalized intensity along the decay direction



Effect of Spatial Distribution on the Formed Pattern

By superimposing three incident light beams with azimuth angles of 0 , $\pi/2$, and π for each beam respectively, pill shape atoms arranging in the square symmetry lattice can be achieved as shown in Fig. 4a. The period of the lattice along the X -direction and the diagonal direction is about 193 and 136 nm, respectively. In addition, it is evident from Fig. 4b, c that the normalized intensity of the E_z component is much higher than that of the E_x component, and there is a phase difference of $\pi/2$ existing between E_z component and E_x component. Thus, the total intensity is dominated by the E_z component. In Fig. 4d, $|E_0|^2$ is the intensity of the incident light. $|E|^2/|E_0|^2$, i.e., the normalized electric field, determines the exposure profile in the photoresist and exponentially decays away from the origin. It should be noted that the interference pattern of the experiment result depends not only on the sensitivity of the photoresist but also on the exposure dosage [5], and the typical threshold value of intensity adopted by conventional lithography is 0.3 [20]. From Fig. 4d, it is clear that by controlling the exposure dosage properly [5], an effective exposure depth of approximately 200 nm can be achieved in the proposed

scheme, which is almost three times of the value of the skin depth (at which the field falls to $1/e$) [20, 25]

$$z_{\text{skin}} = \frac{1}{|k_{z2}|} = \frac{\lambda}{2\pi} \sqrt{\frac{\epsilon_m + \epsilon_d}{\epsilon_m^2}} = 78.2 \text{ nm}$$
 and makes the fabrication of nanostructures by this method more controllable in terms of the working distance.

It should be noted that though the 200-nm effective exposure depth is relatively long, there should be no interference effect in vertical direction as discussed in Reference [5] due to the photoresist thickness set in our simulation which is 300 nm. The thickness of the photoresist is larger than the effective exposure depth means that there should be no reflective electric field intensity reflected from substrate, and therefore, the vertical interference effect does not exist.

Furthermore, by using the required azimuth angle combinations in Table 1, five 2-D Bravais lattices can be achieved. Square, rectangle, rhombic, and oblique lattices are formed by elliptical shape atoms, while hexagonal lattice is formed by circular photonic “atoms.” The intensity profiles of the formed lattices are illustrated in Fig. 5a–e. In addition, the lattice constants calculated from the stimulation result are consistent with the theoretical analysis as well. Moreover, due to the hemispherical prism configuration, it is rather flexible to tune the spatial distribution of three incident

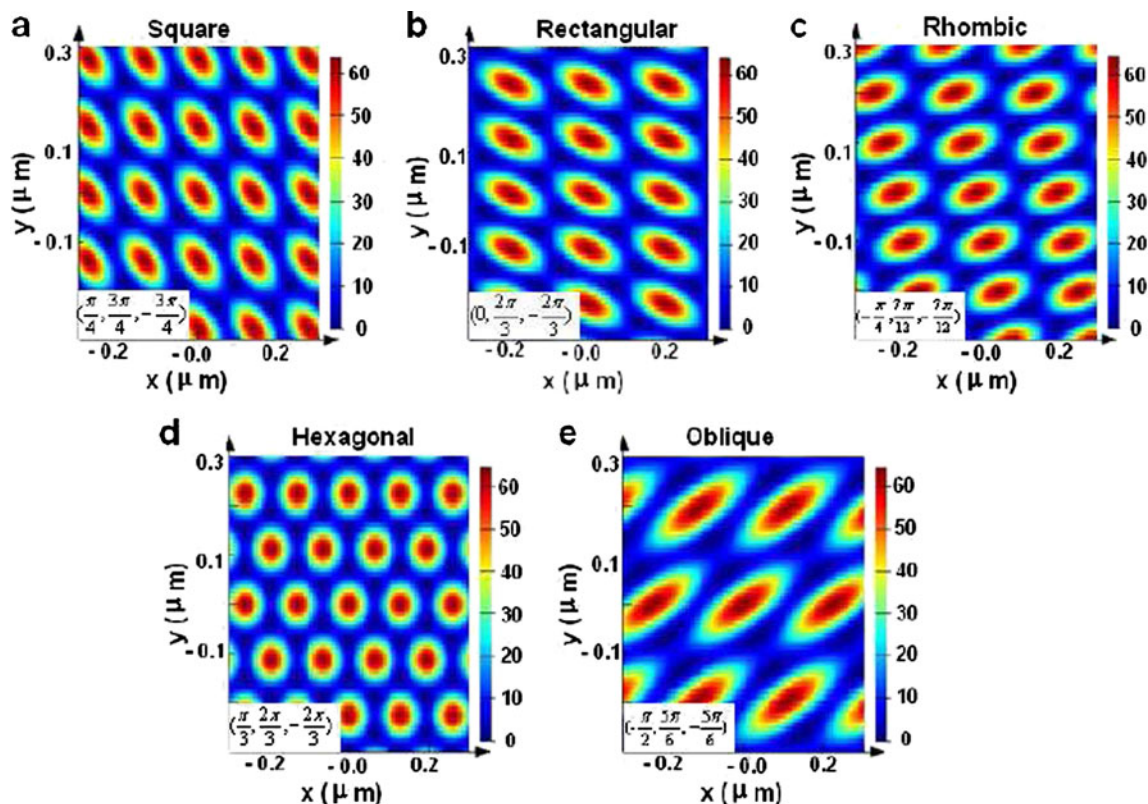
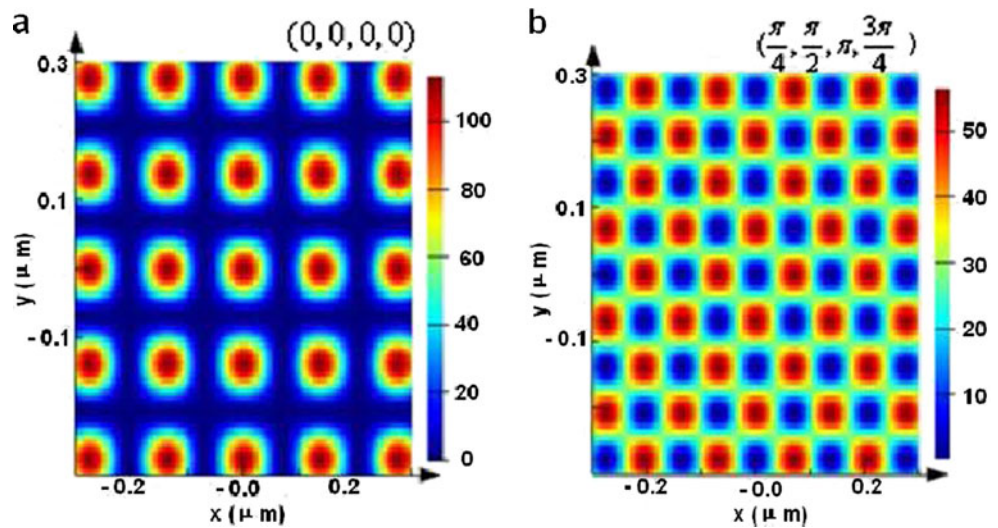


Fig. 5 Intensity profiles of five 2-D Bravais lattices generated by SP holography. The required azimuth angles for each case are shown at the lower left of each pattern. **a** Square. **b** Rectangle. **c** Rhombic. **d** Hexagonal. **e** Oblique

Fig. 6 Four symmetric beams SP holography. Patterns generated on the photoresist layer. The azimuth angles of the incident light are $\pi/4$, $3\pi/4$, $5\pi/4$ and $7\pi/4$, respectively. The initial phases for each case are shown at the *top right* of each pattern

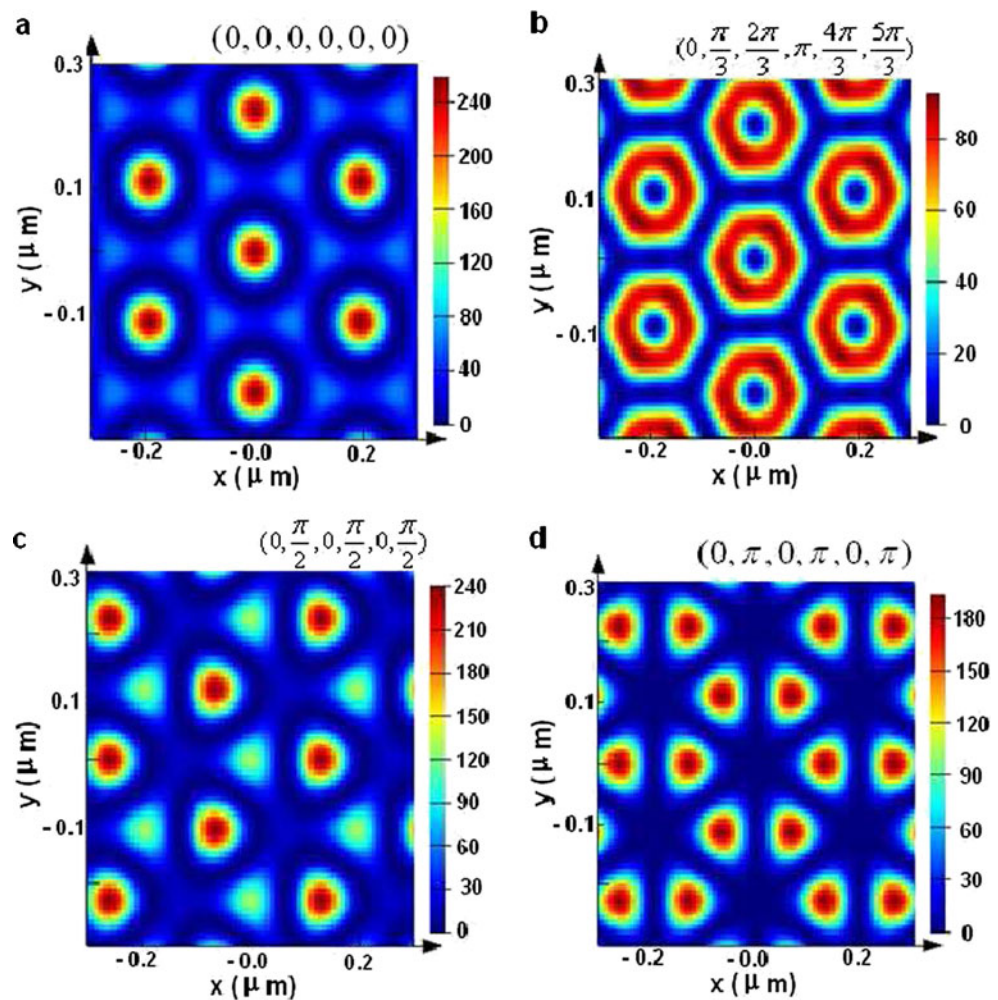


beams to achieve the required azimuth angles when doing experiment. Comparing with the traditional laser holography, the Bravais lattices obtained by SP holography have a higher resolution and aspect ratio.

Effect of Relative Phase on the Formed Pattern

Based on the simulation results, for the case of three-beam SP holography, any variation of the relative phase among the

Fig. 7 Interference profiles of six symmetry beams by SP holography. The azimuth angles of the incident light are $0, \pi/3, 2\pi/3, \pi, 4\pi/3,$ and $5\pi/3$, respectively. The initial phases for each case are shown at the *top right* of each pattern. **a** Hexagonal lattice formed with circular photonic “atoms”. **b** Hexagonal lattice formed with benzene ring-shaped lattice points. **c** Six-petal flower-like lattice structure formed with three stronger non-circular photonic “atoms” and three weaker non-circular photonic “atoms” distributed alternately. **d** Six-petal flower-like lattice structure formed with six equal maximum intensity non-circular photonic “atoms”



three beams leads to similar intensity profile with only a translational shift in the photoresist layer. However, for the case of more than three-beam SP holography, the variation of the relative phase generally leads to different patterns. Figure 6 shows the SP holographic patterns formed by four symmetric beams with equal and unequal initial relative phases. From the stimulation results, it is interesting to see that the formed dots for the unequal initial relative phase are denser and about fourfold of that of the case with equal initial relative phase. In addition, the maximum intensity of the pattern in each row or column shifts about a half of the period according to its neighboring rows or columns. Moreover, the unequal initial relative phase leads to a lower intensity contrast of the holographic pattern, comparing with the equal initial relative phase. However, the period of the dot array in each column or row in Fig. 6a is the same with that of Fig. 6b, i.e., 136 nm.

The holographic patterns formed by six symmetric beams based on SP holography with equal initial phase and unequal initial phases are also studied and illustrated in Fig. 7a–d. It is obvious that the shape of lattice points and lattice structures are different for each case. When the initial phases of the six symmetric beams are equal, a hexagonal lattice with circular photonic “atoms” is formed. When the initial phase of the incident beam is increased with an amount of $\pi/6$ for each beam in turn, a pattern with a hexagonal lattice is formed as well, but each lattice point has a benzene ring shape as shown in Fig. 7b. When the initial phases are set as $(0, \pi/2, 0, \pi/2, 0, \pi/2)$, a six-petal flower-like lattice structure is formed with three stronger non-circular photonic “atoms” and three weaker non-circular photonic “atoms” distributed alternately as shown in Fig. 7c. When the initial phases are set as $(0, \pi, 0, \pi, 0, \pi)$, a six-petal flower-like lattice structure is formed as well, but all of the six non-circular photonic “atoms” have the equal maximum intensity as shown in Fig. 7d. In addition, the intensity contrast changes along with the relative phase changes. However, the period of the lattices in all the above cases always remains the same, i.e., 368 nm in X -direction and 226 nm in Y -direction.

Therefore, by tuning the relative phase difference between incident beams, different forms of periodic patterns can be obtained. It is also worth pointing out that by introducing two or more incident beams with multiple exposures, more other periodic, quasiperiodic, or irregular 2-D lattices with various shapes of lattice points based on the proposed configuration can be obtained as well.

Conclusions

In conclusion, a technique of multiple-beam SP holographic nanolithography with a simple configuration has been analyzed theoretically for the purpose of achieving five 2-D

Bravais lattices photonic crystals and other periodic patterns with a high resolution. Different parameters including the direction of the SP wave vector, the shape of the unit cell, the period of the lattices, and the initial phases of the SP waves can be controlled flexibly by means of properly arranging the spatial distribution of the incident light beams as well as tuning the relative phases among the incident light beams. The simulation results are useful for the practical design of the SP holographic nanolithography for the fabrication of the nanostructures with desired profiles.

Acknowledgments This work is supported by the National Natural Science Foundation of China with grant numbers 90923036, 60977041, 60877021, 11079014, and 61077010 as well as the 100 Talents Program of Chinese Academy of Sciences.

References

- Choi WK, Liew TH, Chew HG, Zhang F, Thomposon CV, Wang Y, Hong MH, Wang XD, Li L, Yun J (2008) A combined top-down and bottom-up approach for precise placement of metal nanoparticles on silicon. *Small* 4(3):330–333
- Choi WK, Liew TH, Dawood MK (2008) Synthesis of silicon nanowires and nanofin arrays using interference lithography and catalytic etching. *Nano Lett* 8(11):2799–2802
- Lim CS, Hong MH, Lin Y, Xie Q, Luk'yanchuk BS, Kumar AS, Rahman M (2006) Microlens array fabrication by laser interference lithography for super-resolution surface nanopatterning. *Appl Phys Lett* 89:191125
- Chong TC, Hong MH, Shi LP (2010) Laser precision engineering: from microfabrication to nanoprocessing. *Laser Photonics Rev* 4(1):123–143
- Xie Q, Hong MH, Tan HL, Chen GX, Shi LP, Chong TC (2008) Fabrication of nanostructures with laser interference lithography. *J Alloy Compd* 449:261–264
- Wang X, Xu JF, Su HM, Zeng ZH, Chen YL, Wang HZ (2003) Three-dimensional photonic crystals fabricated by visible light holographic lithography. *Appl Phys Lett* 83(14):2212–2214
- Lin YK, Harb A, Lozano K, Xu D, Chen KP (2009) Five beam holographic lithography for simultaneous fabrication of three dimensional photonic crystal templates and line defects using phase tunable diffractive optical element. *Opt Express* 17(19):16625–16631
- Jun HM, Seung-M Y (2004) Multiple-exposure holographic lithography with phase shift. *Appl Phys Lett* 85(18):4184–4186
- Liang B, Liu YK, Li JT, Song LY, Li YY, Zhou JY, Wong KS (2012) Fabrication of large-size photonic crystals by holographic lithography using a lens array. *J Micromech Microeng* 22:035013
- Liang GQ, Mao WD, Pu YY, Zou H, Wang HZ (2006) Fabrication of two-dimensional coupled photonic crystal resonator arrays by holographic lithography. *Appl Phys Lett* 89:041902
- Escuti MJ, Crawford GP (2004) Holographic photonic crystals. *Opt Eng* 43(9):1973–1987
- Cai LZ, Yang XL, Wang YR (2002) Interference of three noncoplanar beams: patterns, contrast and polarization optimization. *J Mod Opt* 49(10):1663–1672
- Chua JK, Murukeshan VM, Tan SK, Lin QY (2007) Four beams evanescent waves interference lithography for patterning of two dimensional features. *Opt Express* 15(6):3437–3451
- Sainov S, Anne E, Carole E, Loughnot DJ (2003) High spatial frequency evanescent wave holographic recording in photopolymers. *J Opt A Pure Appl Opt* 5:142–146

15. Ramanujam PS (2003) Evanescent polarization holographic recording of sub-200 nm gratings in an azobenzene polyester. *Opt Lett* 28:2375–2377
16. Martinez-Anton JC (2006) Surface relief subwavelength gratings by means of total internal reflection evanescent wave interference lithography. *J Opt A Pure Appl Opt* 8:S213–S218
17. Sreekanth KV, Murukeshan VM (2010) Large-area maskless surface plasmon interference for one- and two-dimensional periodic nanoscale feature patterning. *Opt Soc* 27(1):95–99
18. Sreekanth KV, Murukeshan VM (2011) Multiple beams surface plasmon interference generation: a theoretical analysis. *Opt Commun* 284:2042–2045
19. Sreekanth KV, Chua JK, Murukeshan VM (2010) Interferometric lithography for nanoscale feature patterning: a comparative analysis between laser interference, evanescent wave interference, and surface plasmon interference. *Appl Opt* 49(35):6710–6717
20. Guo XW, Du JL, Guo YK (2006) Large-area surface plasmon polariton interference lithography. *Opt Lett* 31(17):2613–2615
21. Fang L, Du JL, Guo XW, Wang JQ, Zhang ZY, Luo XG, Du CL (2008) The theoretic analysis of maskless surface plasmon resonant interference lithography by prism coupling. *Chin Phys B* 17(7):2499–2505
22. Luo XG, Ishihara T (2004) Surface plasmon resonant interference nanolithography technique. *Appl Phys Lett* 84(23):4780–4782
23. Zhao-W L, Qi-H W, Xiang Z (2005) Surface plasmon interference nanolithography. *Nano Lett* 5(5):957–961
24. Lim Y, Kim S, Kim H, Jung J, Lee B (2008) Interference of surface plasmon waves and plasmon coupled waveguide modes for the patterning of thin film. *IEEE J Quantum Electron* 44(4):305–311
25. Raether H (1988) *Surface plasmons on smooth and rough surfaces and on gratings*. Springer-Verlag, New York
26. Kazuyoshi K, Koji S (2002) Theoretical understanding of an absorption-based surface plasmon resonance sensor based on Kretschmann's Theory. *Anal Chem* 74(3):696–701
27. Palik ED (1985) *Handbook of optical constants of solids*. Academic, San Diego, California